Stephan Klomberg[1]
Institute for Fundamentals
and Theory in Electrical Engineering,
Christian Doppler Laboratory
for Multiphysical Simulation,
Analysis and Design of Electrical Machines,
Inffeldgasse 18, Graz A-8010, Austria
e-mail: stephan.klomberg@tugraz.at

Ernst Farnleitner
Andritz Hydro GmbH,
Dr.-Karl-Widdmann-Strasse 5,
Weiz A-8160, Austria
e-mail: ernst.farnleitner@andritz.com

Gebhard Kastner
Andritz Hydro GmbH,
Dr.-Karl-Widdmann-Strasse 5,
Weiz A-8160, Austria
e-mail: gebhard.kastner@andritz.com

Oszkár Bíró
Institute for Fundamentals
and Theory in Electrical Engineering,
Christian Doppler Laboratory
for Multiphysical Simulation,
Analysis and Design of Electrical Machines,
Inffeldgasse 18, Graz A-8010, Austria
e-mail: biro@tugraz.at

Characteristics of the Convective Heat Transfer Coefficient at the End Winding of a Hydro Generator

The focus of this paper is a computational fluid dynamics (CFD) analysis of the end winding region of a hydro generator as basis for development of correlations between the convective wall heat transfer coefficient (WHTC) and speed and flow rate parameters. These correlations are used as boundary conditions for thermal networks. Furthermore, there is also a focus on the influence of the numerical settings on the correlations. This work deals with a reduced numerical model which is designed to calculate a hydro generator fast and accurately by using a steady-state simulation with the mixing plane (MP) method. [DOI: 10.1115/1.4028978]

1 Introduction

There are two states-of-the-art methods for designing an electrical machine in relation to the thermal management. The first possibility is the use of thermal and flow networks which are similar to electrical circuits. They illustrate the flow path through a machine and work with lumped parameters at connecting nodes. Networks need input of pressure loss coefficients and convective WHTCs. These parameters are based on approximated formulas [1,2], literature [3], empirical data [4], or CFD simulations [5]. Having to find these parameters is a challenging task when using these networks. However, using thermal and flow networks is a fast and accurate method for the design of the cooling system.

A second approach is the use of CFD. Calculating the 3D flow through a generator offers a wide range of results which can verify the network calculations or create input parameters for them. The effort and the accuracy of a CFD simulation depend strongly on the used numerical model, the calculation approach, and the mesh density. CFD computations result in the description of the detailed flow through the machine and can help to optimize the cooling. Their disadvantage is the large computational effort needed.

A review paper on the design process of the ventilation system of a generator using both networks and CFD computations is Ref. [6]. It describes the implementation of these methods for electrical machines as well as their advantages and disadvantages.

Among the publications applying fluid flow computations of hydro generators, several use a state-of-the-art pole sector model (PSM). For example, Refs. [7] and [8] have modeled one pole-sector of the generator with all end winding bars and stator ducts for this sector. These models have an enormous amount of elements and need a number of days for the calculation. Furthermore, in Ref. [9], an experimental validation of the CFD simulation with conjugate heat transfer (CHT) of a scaled generator model is presented. The CHT method solves the heat conduction in the solid with sources of the electromagnetic losses. Another test rig of a small-scale generator is described in Ref. [10]. The generator has been simulated numerically and the experiment yielded flow measurements and flow visualizations at the inlet and outlet. The simulation and the experiment exhibit qualitative agreement and show the influence of the end winding and inlet geometry on the flow path. Further examples of using the PSM are Refs. [11] and [12]. All these papers are devoted to the pole region and the stator ducts and pay no attention to the winding region of large hydro generators.

The PSM leads to an accurate method, but it is hardly possible to carry out a comprehensive parametric study using it. Indeed, the computation time for a PSM of a whole generator is very time consuming due to the high number of elements.

Following Ref. [6], the purpose of this work is to provide a contribution to the determination of the end winding WHTC as an input parameter in thermal networks. The WHTC is computed using CFD simulations. A parametric study covers the range of parameters most influencing the cooling flow through the end winding bars. These are the mass flow rate, the circumferential velocity of the fan, and the rotational speed. Due to the fact that using a PSM would lead to unacceptable computation times, a reduced model has been developed to simplify the PSM and speed up the simulation.

This paper is structured as follows. After introducing the investigated generator in Sec. 2, Sec. 3 focuses on the numerical simulation with the background theory and methodology of CFD and

[1]Corresponding author.

Contributed by the Heat Transfer Division of ASME for publication in the Journal of Thermal Science and Engineering Applications. Manuscript received November 7, 2013; final manuscript received October 24, 2014; published online November 25, 2014. Assoc. Editor: Jovica R. Riznic.

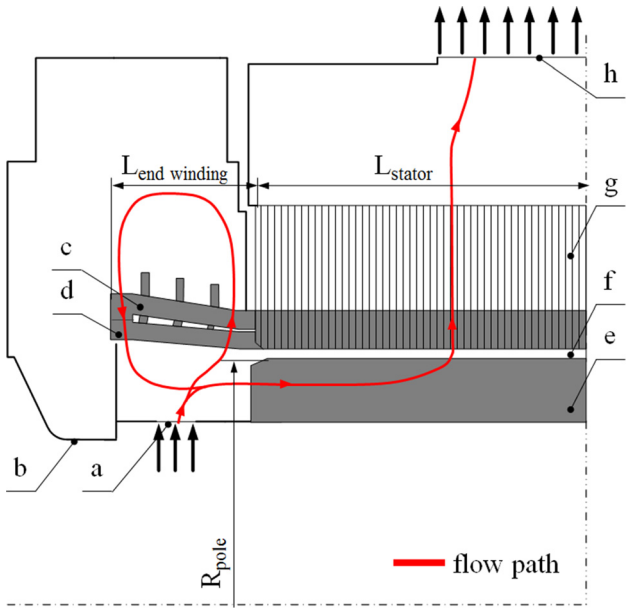

Fig. 1 Longitudinal section of the hydro generator with (*a*) inlet, (*b*) air guide inlet, (*c*) end winding bar bottom, (*d*) end winding bar top, (*e*) salient pole, (*f*) air-gap, (*g*) stator ducts, (*h*) air guide outlet, (*i*) outlet

the explanation of the reduced model. Section 4 will show the results of the numerical investigation and an estimation of its accuracy.

2 Hydro Generator Investigated

The hydro generator presented in Fig. 1 is ventilated by a radial fan. The fan is not modeled, because this part would produce a large number of elements and further increase the calculation time. The estimated flow parameters of the ventilator are given to cover a normal cooling operating field of the hydro generator. These parameters are the circumferential speed, the volume flow rate at the outlet of the fan, and the rotational speed of the rotor. This reduction is the first point to save elements and computing resources. Other simplifications will be described in Sec. 3. Table 1 shows some important technical values of the machine.

3 Methodology of the Reduced Model

The dimensions of a generator can reach up several meters and contain a large fluid volume. This volume is split into smaller subdomains to analyze the fluid flow and heat transfer by means of partial differential equations. As a result of these considerations, the number of elements can be more than 100×10^6 to get accurate results. Figure 2 shows a symmetrical half of a large hydro generator in the axial direction with the most important components.

Due to the large frame size of hydro generators, it makes sense to use the symmetries of the machine and reduce the model geometry. A generator is assumed symmetric in axial and circumferential direction. The model has the dimension of one pole sector after these simplifications.

Table 1 Technical details of the typical medium-sized hydro generator

$L_{\text{end winding}}$	0.5–2 m
L_{stator}	1–4 m
R_{pole}	>1.0 m
Rated power	40–250 MVA

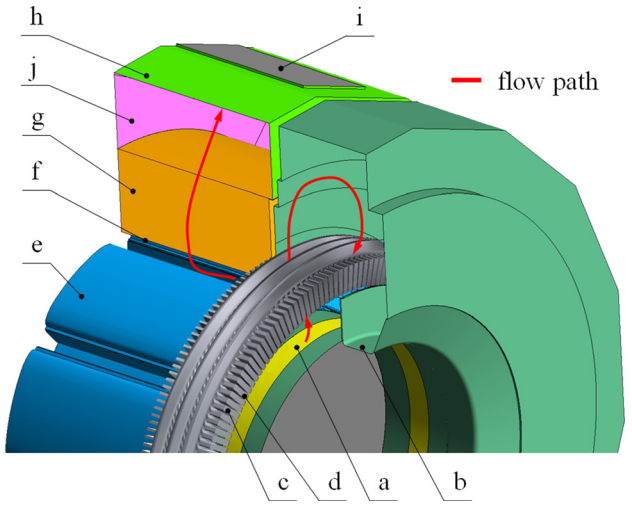

Fig. 2 Schematic model of one axial half of a hydro generator: (*a*) inlet, (*b*) air guide inlet, (*c*) end winding bar bottom, (*d*) end winding bar top, (*e*) salient pole, (*f*) air-gap, (*g*) stator ducts, (*h*) air guide outlet, (*i*) outlet, (*j*) axial symmetry

The second step is the reduction of this state-of-the-art PSM. The idea has been to reduce every component to its minimal required circumferential extension. Therefore, the domains inlet and rotor have a circumferential range of one pole. The domains top bar, bottom bar, stator ducts, and outlet area are reduced to one slot sector. This reduced model is illustrated in Fig. 3. Periodic interfaces are used in circumferential direction and the multiple frames of reference-MP application (MFR-MP) between the domains. The ribs on the surface of the poles have been neglected to simplify the model. This is permissible since the heat flow at the pole surfaces does not substantially influence the heat transfer at the end windings which is in the focus of this work. For the same reason, all solid walls have been assumed to be smooth without a roughness.

In consequence of the mentioned facts, it is possible to save millions of elements in zones of less focus in this work and invest it in the end winging zone, which is of most interest here. The current reduced model has about 3×10^6 elements while a PSM

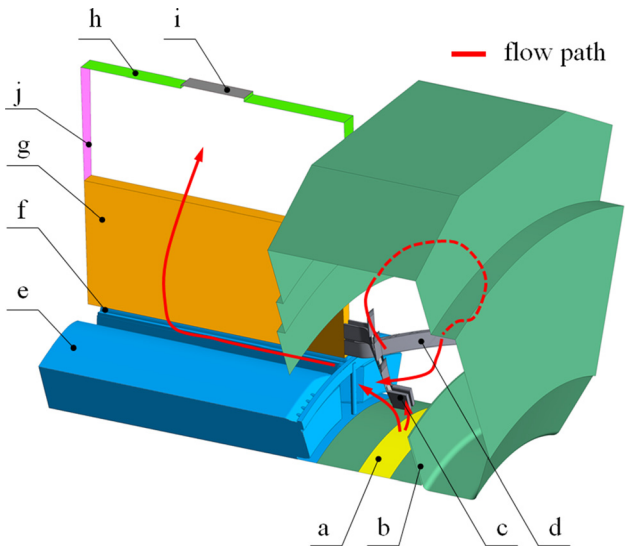

Fig. 3 Reduced slot sector model a hydro generator: (*a*) inlet, (*b*) air guide inlet, (*c*) end winding bar bottom, (*d*) end winding bar top, (*e*) salient pole, (*f*) air-gap, (*g*) stator ducts, (*h*) air guide outlet, (*i*) outlet, (*j*) axial symmetry

would have about 30×10^6 elements. Further on, the accuracy of a CFD calculation of a large hydro generator depends on the corresponding wall treatment and the used turbulence model (see Secs. 3.2 and 3.3).

The calculations have been done with the commercial software package ANSYS-CFX-14.5 [13] and the mesh generation with ANSYS-ICEM-CFD-13.0 [14]. The simulation time for one operating point is about 1–2 days on an Intel Xeon with a 12 cores/3.47 GHz/192 GB RAM server setup. A 64-bit operating system and four cores of the processor have been used for the calculation.

3.1 Rotor–Stator Interaction (RSI) Strategy. A special challenge was to find the best RSI strategy to connect the reduced components and get numerically stable and convergent results. The most common RSI method is the MFR-frozen rotor application (MFR-FR). This is a relatively fast and accurate technique which is used, e.g., in Refs. [5–12] and [15]. This type of interface switches between the rotating and the stationary frame of reference and commits the flow field from the rotor to the stator.

A second option is the MFR-MP technique. The flow data are circumferentially averaged on bands at the upstream side of the interface. Afterward, the averaged physical values are committed to the downstream component. A schematic sketch is shown in Fig. 4. For example, a passage can be a fixed (stator) and rotating (rotor) blade of a turbine or an end winding bar (stator) and the appropriate pole section (rotor) of an electrical machine. This alternative has the advantage of using large pitch ratios between the rotor and the stator, wherefore the number of elements can be reduced. These two RSI-methods are compared in Refs. [7] and [11] for the calculation of the flow conditions between the rotor and the stator ducts. The fundamental numerical methods for this strategy have been developed and tested for the simulation of compressors, turbines, and pumps in Refs. [16–18]. These publications show that the steady-state MP approach is an accurate alternative to transient and MFR-FR simulations.

The implementation of large pitch ratios in combination with the MP interface is used in this work to yield average results of the WHTC at the end winding bars. The pitch ratio is defined in Eq. (1) as the ratio of the angles of two domains. The different angles of the domains are also shown in Fig. 5.

$$p = \frac{p_R}{p_S} \tag{1}$$

The obvious advantages of the MP method are the large possible pitch ratio and the averaging on bands. Knowing the

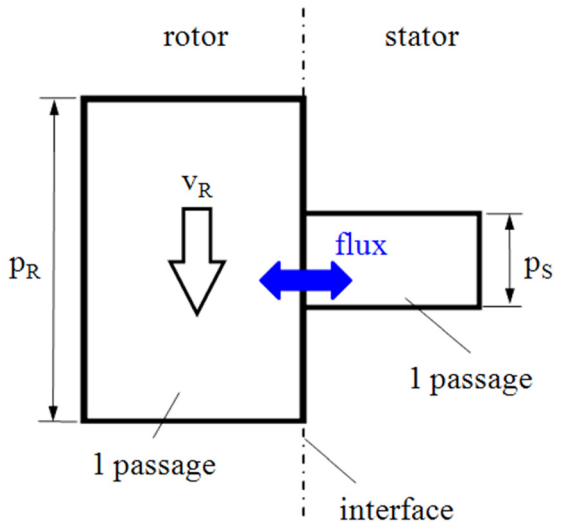

Fig. 4 Sketch of simple RSI-MP

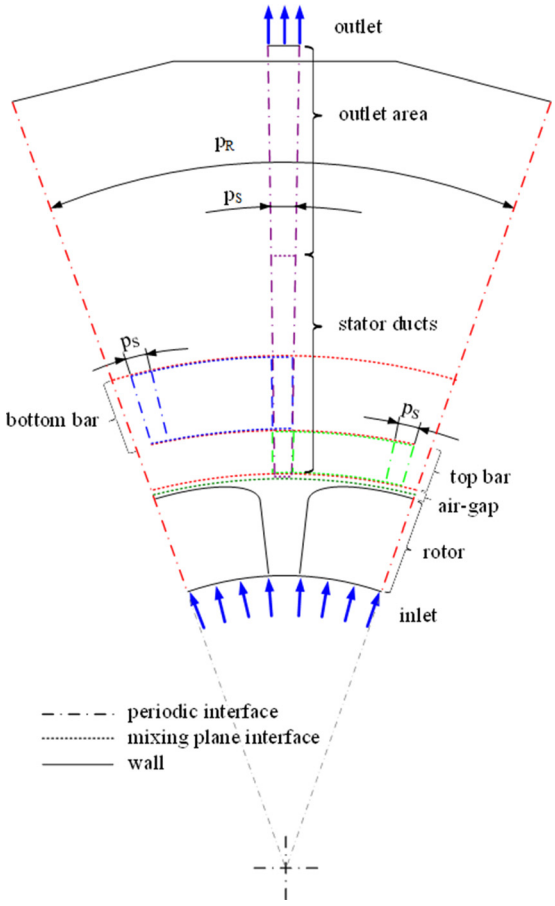

Fig. 5 Front view reduced model

circumferential average of velocity, pressure or temperature is sufficient to determine the WHTC at the end winging bars. The detection of spatial vortices or stalls is of less importance for this work. Accordingly, the simulation time for a large hydro generator can be reduced enormously. A disadvantage is the numerical instability during the first hundred iterations. The numerical instability is caused by a large velocity gradient in the elements in the area of the connection of the domains inlet, top bar, rotor, and stator ducts domain. The domain inlet, rotor, and stator ducts have a coarse mesh contrary to the fine mesh of the top bar. This rapid transition of a fine mesh to a coarse mesh causes the numerical instabilities. The difficulty was adjusting the right time step for the simulation. Therefore, a larger time step is used at the beginning and has to be reduced after 100–150 iterations to get a stable and settled numerical residuum. The time step for a rotational machine should be around $1/n$. The tendency of numerical instabilities of the MFR-MP method for the simulation of generators has been also detected by Toussaint et al. [7].

3.2 Turbulence Model. The Reynolds-averaged Navier–Stokes (RANS) equations are time-averaged equations to describe turbulent flows. Turbulence models are necessary to close these RANS equations [19]. The choice of the appropriate turbulence model has a major effect on the results. In the last decades many models have been developed or improved. A comparison of various turbulence models using a simple arrangement of a circular cylinder is presented in Ref. [15]. It turns out that the shear-stress-transport (SST) turbulence model fits best to the measurement results. The authors have then transferred this finding to the simulation of the heat transfer at the end winding of a totally enclosed fan cooled (TEFC) induction machine. Their measurements of the heat transfer in this machine have shown that the trends of

measured and numerical results are the same. The SST turbulence model combines the best parts of the k-ε and the k-ω models [20]. The k-ω model is used in the boundary layer near the walls. The SST model automatically switches to the k-ε model in the free stream away from the wall using a blending function based on the flow variables and the distance to the nearest surface.

A study of different test cases is shown in Ref. [21]. This study compares the three models k-ε, k-ω, and SST with experimental data for some important technical applications. The very good accuracy of the SST turbulence model with the appropriate wall function is also demonstrated. Consequently, all simulations in this paper have been carried out using the SST model.

3.3 Wall Treatment and Mesh Density. The dimensionless distance from the wall has a strong impact on the WHTC. The height of the first element adjacent to the wall Δy should be as small as possible to minimize y^+, the dimensionless distance from the wall as defined in Eq. (2) where ν is the kinematic viscosity, τ_W is the wall shear stress, and ρ is the density.

$$y^+ = \sqrt{\frac{\tau_W}{\rho}} \cdot \frac{\Delta y}{\nu} \tag{2}$$

The automatic near-wall treatment is used as required by the SST turbulence model. This method switches automatically from wall functions to a low-Reynolds near wall formulation. The blending function for the velocity profile near the wall is described in Eqs. (3)–(6). It shows the relation between the velocity in the first cell adjacent to the wall U_1 and the wall shear stress τ_W. κ is the von Karman constant and C is a log-layer constant depending on the wall roughness. Further detailed descriptions can be found in Refs. [21] and [22].

$$u_\tau = \left(\frac{\tau_W}{\rho}\right)^{\frac{1}{2}} \tag{3}$$

$$u_\tau = \sqrt[4]{\left(u_\tau^{vis}\right)^4 + \left(u_\tau^{log}\right)^4} \tag{4}$$

$$u_\tau^{vis} = \frac{U_1}{y^+} \tag{5}$$

$$u_\tau^{log} = \frac{U_1}{\frac{1}{\kappa} \cdot \ln(y^+) + C} \tag{6}$$

It is recommended in Ref. [21] to use a value of about 1 for y^+. Regarding these publications, it is important to consider that very small cells can lead to convergence problems; especially in regions with high velocity gradients (see also Sec. 3.1). In this context, a comparison of two y^+ values and their influence on the WHTC is carried out in Sec. 4.2.

The first reduced model has a total mesh size of 5×10^6 hexahedral elements. About 3.3×10^6 elements can be dedicated to the domains inlet area, rotor, stator ducts, and outlet area. The remaining 1.7×10^6 elements are used in the top and bottom bar domain. The averaged y^+ at the wall of the end winding bars is about 1. A second mesh generated has a y^+ of nearly 8. The total mesh size is 2.7×10^6 elements of which 0.6×10^6 are used for the end winding bars. Figure 6 shows the comparison of the mesh at the topside of 2 bars. The left side is the mesh with a y^+ of 8. The first cell at the wall has a height of 0.25 mm and the number of elements between the 2 bars is about 26. On the right side the mesh with a y^+ of around 1 is shown. Therefore, the number of elements is 50 and the height Δy is 0.05 mm. The growth from the wall is defined with a Poisson distribution for both meshes. The mesh around the components bars, support rings, and space brackets is shown in Fig. 7, too. This is the mesh with a y^+ of about 1.

The heat transfer at the walls of the inlet area, rotor, stator ducts, and outlet area has not been investigated in this work. Therefore, the mesh density near these walls is coarse.

3.4 Fluid Properties. The standard setting in ANSYS-CFX-14.5 for an ideal gas is temperature independent, i.e., the thermal conductivity λ, the specific heat capacity c_p, and the dynamic viscosity μ are constant. This is a simplification which may lead to inaccurate results. An ideal temperature dependent gas has been modeled and compared to a temperature independent ideal gas in Ref. [23]. As shown there, the differences in the heat transfer are negligible.

The temperature dependence of the dynamic viscosity and the thermal conductivity are modeled with Sutherland's formula in Eqs. (7) and (8). The reference temperature T_R has been set to 325 K. The reference molecular viscosity μ_0, the reference molecular conductivity λ_0, the Sutherland constants S_λ/S_μ, and the temperature exponent's n_λ/n_μ are also specified in Eqs. (7) and (8). The temperature dependence of the specific heat capacity is approximately the zero pressure polynomial in Eq. (9). These correlations are described more accurate in Ref. [13]. All physical values have been found by automatically adjusting them to measured thermodynamic properties of dry air gathered in Ref. [24]. These values are valid in a temperature range from 260 K to 670 K.

$$\frac{\mu}{\mu_0} = \frac{T_R + S_\mu}{T + S_\mu} \cdot \left(\frac{T}{T_R}\right)^{n_\mu} \tag{7}$$

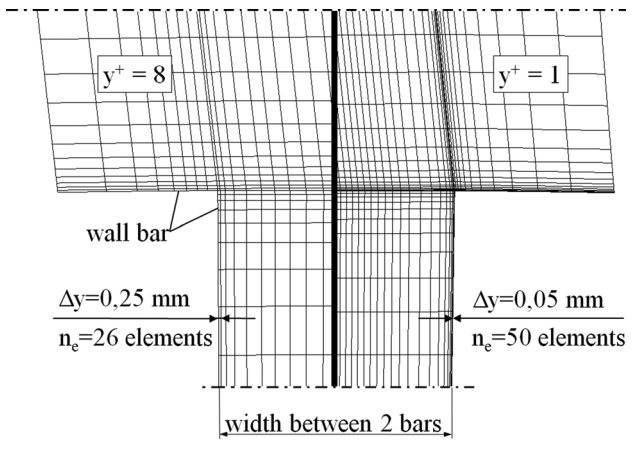

Fig. 6 Comparison of the two used grids around the end winding bar

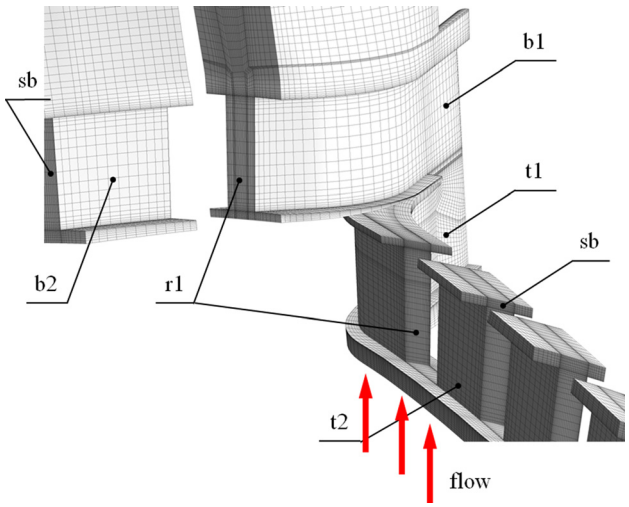

Fig. 7 Mesh of the domain end winding bars. $y^+ \approx 1$.

$$\frac{\lambda}{\lambda_0} = \frac{T_R + S_\lambda}{T + S_\lambda} \cdot \left(\frac{T}{T_R}\right)^{n_\lambda} \tag{8}$$

where $S_\mu = 77.8\,\text{K}$, $\mu_0 = 1.972 \times 10^{-5}\,\text{Pa}\cdot\text{s}$, $n_\mu = 1.574$, $S_\lambda = 60.7\,\text{K}$, $\lambda_0 = 2.82 \times 10^{-2}\,\text{W/m}\cdot\text{K}$, and $n_\lambda = 1.676$.

$$\frac{c_p}{R_S} = t_1 + t_2 \cdot T + t_3 \cdot T^2 + t_4 \cdot T^3 + t_5 \cdot T^4 \tag{9}$$

where $R_S = 287.058\,\text{J/kg}\cdot\text{K}$, $t_1 = 3.574$, $t_2 = -4.2691 \times 10^{-4}$, $t_3 = -4.1854 \times 10^{-8}$, $t_4 = 3.0986 \times 10^{-9}$, and $t_5 = -2.3848 \times 10^{-12}$.

3.5 Analysis Requirement. Some important facts have to be clarified before discussing the results. The aim of this paper is the calculation of the convective WHTC at the end winding bars. The wall heat flux density has been calculated by CFD. The wall temperature of the end winding bars T_W and the reference temperature T_{Ref} are fixed. The WHTC (h) is defined as

$$h = \frac{\dot{q}_W}{T_W - T_{Ref}} \tag{10}$$

As the solid part is not calculated by CHT, the wall temperature is set as a boundary condition for every wall. This simplification reduces the number of elements and the simulation time, too. The wall temperatures for the various walls of the generator have been defined on the basis of empirical values wherefore the heat flux is computed realistically. The boundary conditions at the inlet are the radial speed v_r and the circumferential speed v_u and at the outlet a static pressure p_{Stat}. The rotational speed n is given for the rotating part, too. Table 2 shows the values of the boundary conditions.

Figure 8 shows the classification of an end winding bar which is split up into six zones for the subsequent analysis. These subsections are located between the support rings (r1–r2) and the space brackets (sb1, sb2). These two components serve the mechanically support of the end windings. The flow phenomena

Table 2 Boundary conditions of the model

T_{Ref}	(K)	313
T_W	(K)	393
v_u	(m/s)	30–100
v_r	(m/s)	12–18
N	(rpm)	500–1000
p_{Stat}	(Pa)	0

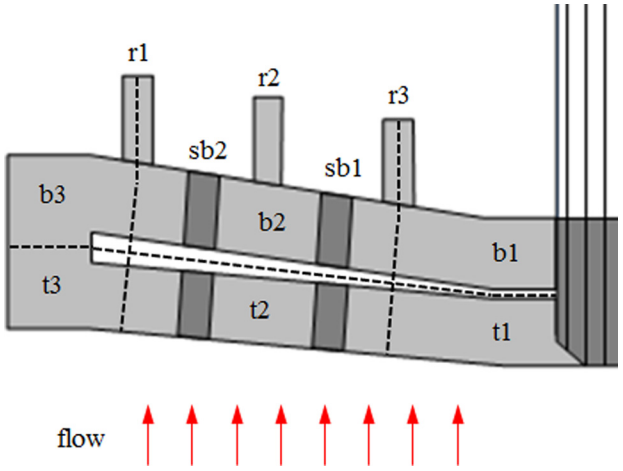

Fig. 8 Classification of an end winding bar

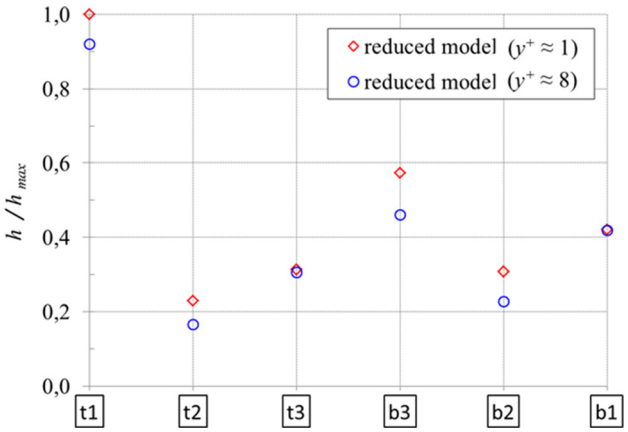

Fig. 9 Characterization of the WHTC along an end winding bar

in the surroundings of the end winding influence the heat transfer to a large extent.

4 Discussion of the Results

4.1 Mesh Comparison. Based on the results of the parameter study with two different reduced models, Fig. 9 shows the WHTC along an end winding bar. The WHTC is normalized with the maximum value of the WHTC along the bar. The results are shown for the two meshes described in Sec. 3.3. The value $y^+ \approx 1$ results in higher WHTC than the model with $y^+ \approx 8$. This difference is a result of the insufficient resolution of the flow field for the automatic wall treatment at $y^+ \approx 8$ leading to too low near wall velocity and hence to lower WHTC [21].

However, the difference between the two results is not substantial and the model with a coarser mesh has the advantage of a faster calculation time. This model needs less than half of the time of the one with $y^+ \approx 1$. Moreover, the numerical instabilities are less pronounced, too. A fundamental mesh study has been presented in Ref. [23]. As shown there, the WHTC increases with decreasing y^+, reaching its peak at $y^+ \approx 8$ and fluctuating around this maximum for lower y^+ values. This behavior of y^+ is also

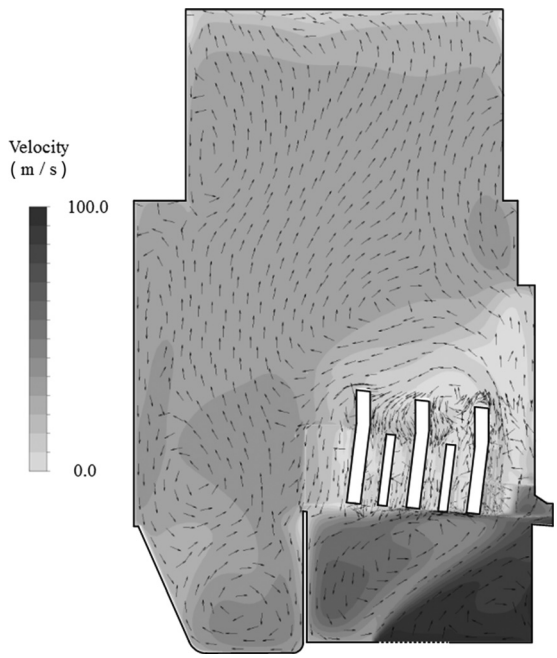

Fig. 10 Typical flow condition at the inlet area

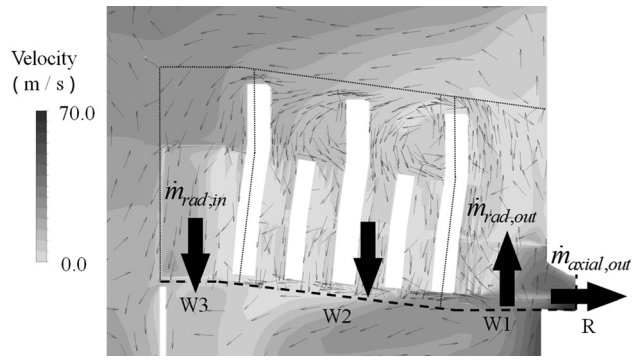

Fig. 11 Flow velocity distribution at the end winding cross section

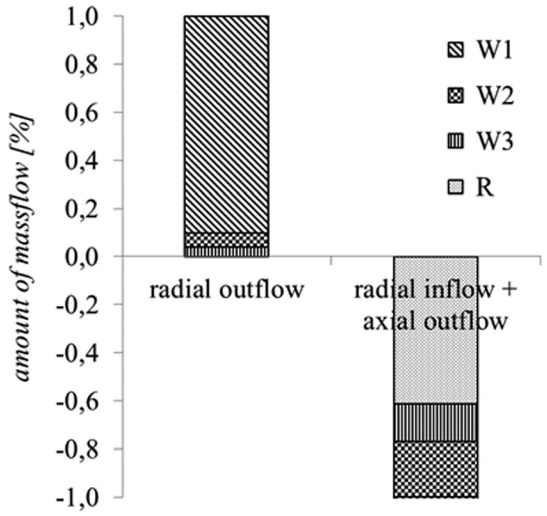

Fig. 12 Distribution of the radial outflow and inflow, and axial outflow through the end winding bars

shown in Ref. [11] for a mesh study at the stator ducts of a large hydro generator. Hence, the coarser mesh ($y^+ \approx 8$) will be used for the parametric study in Sec. 4.3.

4.2 Flow Conditions. Figure 10 illustrates the typical flow conditions of the investigated fan cooled generator. A cross

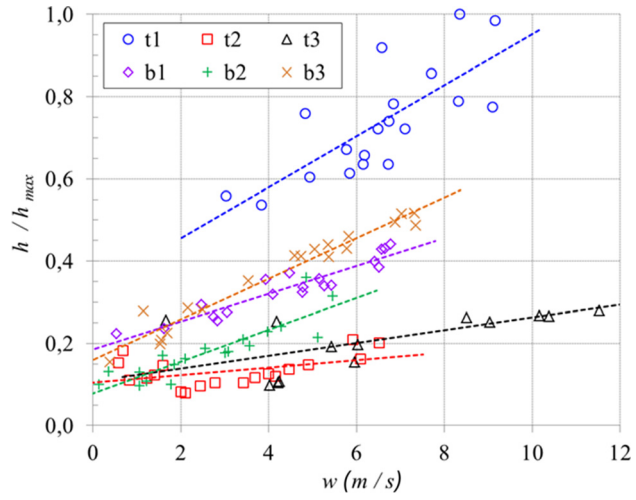

Fig. 13 Comparison of the WHTC with the radial velocity in the evaluation zones

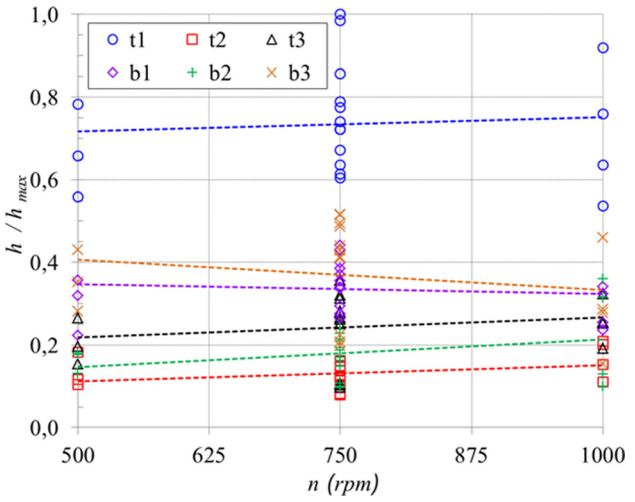

Fig. 14 Comparison of the WHTC for different rotational speed

section of the inlet and end winding domains is shown with the velocity contour and the appertaining vectors.

The inflow splits off in two different cooling paths. The main flow streams directly in the rotor and through the stator ducts to the outlet. A subcooling path makes a loop through the end winding and then merges with the main path in the rotor. The rotor works like the impeller of a pump or compressor and provides a suction of the air in axial direction. Therefore, the main cooling flow of the end winding is through the control zones t1 and b1.

It is obvious that the velocity in the other bar regions is smaller, especially in the zones t2, b2, and t3. Hence, the WHTC is smaller than in t1. This effect is shown clearly in Fig. 9.

The 2D flow distribution at the end winding domain is shown in Fig. 11. The bar graph in Fig. 12 presents the distribution of the radial outflow $\dot{m}_{\mathrm{rad,out}}$, inflow $\dot{m}_{\mathrm{rad,in}}$, and axial outflow $\dot{m}_{\mathrm{axial,out}}$ in the end winding domain. The radial outflow is cold air from the fan which streams through the bar domain upward mainly in W1. The radial inflow is the backflow through the control surfaces W2 and W3. The axial control area R is the transition to the air-gap. A large amount of air channels off into the air-gap after passing W1. The simulation results indicate a high velocity at the top bar zone t1, but the speed decelerates with increasing radius. The radial inflow velocity at b2, t2, and t3 is less because of the lower mass flow.

4.3 Parametric Study. Results of the parametric study are shown in Figs. 13 and 14. The WHTC is also made nondimensional by the maximum value of the WHTC along the bar for these figures. Figure 13 presents the WHTC for the six different zones as a function of the radial velocity between the bars. The cold air streams first through the zones t1 and b1. Due to this, t1 and b1 have the highest WHTC. Vortices around b3 result in a high WHTC in this zone, too. All other zones exhibit very small WHTC values because of the warmer backflow of the air. This flow behavior is also illustrated in Figs. 10 and 11.

Other important parameters are the inlet swirl and the rotational speed. The inlet swirl influences the flow through the bars directly and therefore the radial velocity w. Figure 14 shows the variation of the WHTC with the rotational speed. The minimal linear progression of the curves indicates a low dependence on the cooling and the rotational speed. Due to this, the velocity between the bars is the most dominating parameter for the cooling of the end winding bars.

5 Conclusion

This paper has presented an approach for a fast, stable, and accurate flow calculation of a large hydro generator. The new

simplified numerical model has reduced the components to their minimal required circumferential extensions. The MP technique has been used to connect the domains of the model. Numerical instabilities can occur if the time step is not properly chosen. This problem is solved by using different time steps during the simulation runs.

One central investigation describes the influence of the dimensionless distance from the wall and the mesh density on the heat transfer. It has been confirmed that a $y^+ \approx 1$ is desirable but not mandatory. The results of the mesh and parameter study show a highly nonuniform WHTC distribution along the end winding bars. The best cooled zones are t1 and b1. The rotational speed does not influence the WHTC.

One possible future work could focus on improvements concerning a homogenization of the wall heat transfer distribution; i.e., the flow to the bars is the same in every zone and the WHTC is approximately the same along the bar. Another major future topic is the extension of the parametric study with the geometrical influence of the inlet (fan) to get a correlation between the WHTC and the flow rate parameters and the geometrical parameters. These correlations of the WHTC will build a basis for the boundary conditions of thermal networks.

Acknowledgment

The authors wish to thank Andritz Hydro GmbH for permission to publish this work.

This work has been supported by the Christian Doppler Research Association.

Nomenclature

Latin Symbols

C = log-layer constant
c_p = specific heat capacity (J/kg · K)
CFD = computational fluid dynamics
CHT = conjugate heat transfer
h = wall heat transfer coefficient (W/m^2 · K)
h_{max} = maximum wall heat transfer coefficient of parametric study (W/m^2 · K)
$L_{end\ winding}$ = length of the end winding bars (m)
L_{stator} = length of the stator (m)
MFR-FR = multiple frames of reference-frozen rotor
MFR-MP = multiple frames of reference-mixing plane
n = rotational speed of the rotor
n_e = number of elements between 2 bars
n_λ = temperature exponent for molecular conductivity
n_μ = temperature exponent for molecular viscosity
p = pitch ratio
p_R = pitch inlet, rotor (rad)
p_S = pitch end winding bars, stator ducts, outlet (rad)
p_{Stat} = static pressure (Pa)
$\dot{q}_W$ = wall heat flux density (W/m^2)
R_{fan} = radius fan (m)
R_{pole} = radius pole (m)
R_S = specific gas constant (J/kg · K)
RANS = Reynolds-averaged Navier–Stokes
RSI = rotor–stator interaction
S_λ = Sutherland constant for molecular conductivity
S_μ = Sutherland constant for molecular viscosity
SST = shear-stress-transport
T = temperature of the dry air (empirical data) (K)
t_1–t_5 = coefficients
T_R = reference temperature for ideal gas calculation (K)
T_{Ref} = reference temperature of the fluid for WHTC (K)
T_W = wall temperature (K)
TEFC = totally enclosed fan cooled
u_τ = friction velocity (m/s)
U_1 = velocity in the first cell adjacent to the wall (m/s)
u_τ^{log} = friction velocity in the logarithmic region of the turbulent boundary layer (m/s)
u_τ^{vis} = friction velocity in the viscous sublayer of the turbulent boundary layer (m/s)
v_R = radial velocity at the inlet (m/s)
v_u = circumferential velocity at the inlet (m/s)
w = radial velocity in the evaluation zones between bars (m/s)
WHTC = wall heat transfer coefficient (W/m^2 · K)
y^+ = dimensionless distance from the wall
2D = two-dimensional
3D = three-dimensional

Greek Symbols

Δ_y = height of first element adjacent to the wall (m)
κ = von Karman constant
λ = thermal conductivity (W/m · K)
λ_0 = reference molecular conductivity (W/m · K)
μ = dynamic viscosity (Pa · s)
μ_0 = reference molecular viscosity (Pa · s)
ν = kinematic viscosity (m^2/s)
ρ = density (kg/m^3)
τ_W = wall shear stress (N/m^2)

References

[1] Gerling, D., and Dajaku, G., 2005, "Novel Lumped-Parameter Thermal Model for Electrical Systems," Proceedings of European Conference on Power Electronics and Applications, Dresden, Germany.
[2] Boglietti, A., Cavagnino, A., and Staton, D., 2008, "Determination of Critical Parameters in Electrical Machine Thermal Models," IEEE Trans. Ind. Appl., **44**(4), pp. 1150–1159.
[3] Idelchik, I. E., 1986, *Handbook of Hydraulic Resistance*, 2nd ed., Hemisphere Publishing Corporation, Washington, DC.
[4] Boglietti, A., Cavagnino, A., Staton, D. A., Popescu, M., Cossar, C., and McGilp, M. I., 2008, "End Space Heat Transfer Coefficient Determination for Different Induction Motor Enclosure Types," IEEE Trans. Ind. Appl., **45**(3), pp. 929–937.
[5] Micallef, C., Pickering, S. J., Simmons, K. A., and Bradley, K. J., 2008, "Improved Cooling in the End Region of a Strip-Wound Totally Enclosed Fan-Cooled Induction Electric Machine," IEEE Trans. Ind. Electron., **55**(10), pp. 3517–3524.
[6] Farnleitner, E., and Kastner, G., 2010, "Moderne Methoden der Ventilationsauslegung von Pumpspeichergeneratoren," e&i Elektrotech. Informationstech., **127**(1), pp. 24–29.
[7] Toussaint, K., Torriano, F., Morissette, J.-F., Hudon, C., and Reggio, M., 2011, "CFD Analysis of Ventilation Flow for a Scale Model Hydro Generator," ASME Paper No. POWER2011-55202.
[8] Dépraz, R., Zickermann, R., Schwery, A., and Avellan, F., 2006, "CFD Validation and Air Cooling Design Methodology for Large Hydro Generator," Proceedings of 17th International Conference on Electrical Machines ICEM, Greece.
[9] Ujiie, R., Arlitt, R., and Etoh, H., 2005, "Application of Computational Fluid Dynamics on Ventilation-Cooling Optimization of Electrical Machines," Colloquium on Large Electrical Machines CIGRE-EPFL, Lausanne.
[10] Moradnia, P., Chernoray, V., and Nilsson, H., 2012, "Experimental and Numerical Study of Cooling Air Flow in a Hydroelectric Generator," Proceedings of 9th International ERCOFTAC Symposium on Engineering Turbulence Modeling and Measurements, Thessaloniki, Greece.
[11] Schrittwieser, M., Marn, A., Farnleitner, E., and Kastner, G., 2014, "Numerical Analysis of Heat Transfer and Flow of Stator Duct Models," IEEE Trans. Ind. Appl., **50**(1), pp. 226–233.
[12] Houde, S., Hudon, C., and Vicent, P. B., 2008, "Simulation Strategies of the Cooling Flow for Large Hydro Generators," Hydropower Dams, **15**(6), pp. 93–99.
[13] 2012, "ANSYS CFX Documentation," ANSYS, Inc., Canonsburg, PA, Release 14.5.
[14] 2010, "ANSYS ICEM CFD Documentation," ANSYS, Inc., Canonsburg, PA, Release 13.0.
[15] Hettegger, M., Streibl, B., Bíró, O., and Neudorfer, H., 2012, "Measurements and Simulations of the Convective Heat Transfer Coefficients on the End Windings of an Electrical Machine," IEEE Trans. Ind. Electron., **59**(5), pp. 2299–2308.
[16] Galpin, P., Broberg, R., and Hutchinson, B., 1995, "Three-Dimensional Navier-Stokes Predictions of Steady State Rotor-Stator Interaction With Pitch Change,"

Proceedings of 3rd Annual Conference of the CFD Society of Canada, Banff, AB, Canada.
[17] Belamri, T., Galpin, P., Braune, A., and Cornelius, C., 2005, "CFD Analysis of a 15 Stage Axial Compressor Part I: Methods," ASME Paper No. GT2005-68261.
[18] Belamri, T., Galpin, P., Braune, A., and Cornelius, C., 2005, "CFD Analysis of a 15 Stage Axial Compressor Part II: Results," ASME Paper No. GT2005-68262.
[19] Oertel, H., 2004, *Prandtl's Essentials of Fluid Mechanics*, 2nd ed., Springer-Verlag, New York.
[20] Menter, F. R., 1994, "Two-Equation Eddy-Viscosity Turbulence Models for Engineering Applications," AIAA J., **32**, pp. 1598–1605.
[21] Vieser, W., Esch, T., and Menter, F. R., 2002, "Heat Transfer Predictions Using Advanced Two-Equation Turbulence Models," CFX Technical Memorandum, AEA Technology, Otterfing, Germany.
[22] Kader, B. A., 1981, "Temperature and Concentration Profiles in Fully Turbulent Boundary Layers," Int. J. Heat Mass Transfer, **24**(9), pp. 1541–1544.
[23] Klomberg, S., Farnleitner, E., Kastner, G., and Bíró, O., 2012, "Heat Transfer Analysis on End Windings of a Hydro Generator Using a Stator-Slot-Sector Model," Proceedings of 14th International IGTE Symposium on Numerical Field Calculation, Graz.
[24] Kreith, F., Manglik, R. M., and Bohn, M. S., 2011, *Principles of Heat Transfer*, 7th ed., Cengage Learning, Stamford, CT.